RSC Advances

PAPER

View Article Online
View Journal | View Issue

Cite this: *RSC Adv.*, 2020, **10**, 33770

Nanostructured cobalt antimonate: a fast responsive and highly stable sensing material for liquefied petroleum gas detection at room temperature

Satyendra Singh, *[a] Archana Singh,[b] Ajendra Singh,[b] Sanjeev Rathore,[c] B. C. Yadav[d] and Poonam Tandon *[b]

Herein, cobalt antimonate ($CoSb_2O_6$) nanospheres were fabricated *via* the sol–gel spin-coating process and employed as a functional liquefied petroleum gas (LPG) sensor at room temperature (25 °C). The microstructure of the fabricated $CoSb_2O_6$ thin films (thickness ~ 250 nm) was analyzed *via* scanning electron microscopy, which revealed the growth of nanospheres having an average diameter of ~45 nm. The XRD analysis demonstrated the crystalline nature of $CoSb_2O_6$ with a crystallite size of ~27 nm. Finally, the fabricated thin films were investigated as sensors for LPG and carbon dioxide (CO_2) at room temperature (25 °C) and 55% R.H. (relative humidity) with different concentrations in the range of 1000–5000 ppm. The sensing results demonstrated greater variations in the electrical properties of films for the incoming LPG than that of the CO_2 gas adsorption. Furthermore, to ensure the long-term stability of fabricated sensors, they were tested periodically at 10 days interval, spanning a total duration of 60 days. In summary, our fabricated LPG sensor displayed high sensitivity (1.96), repeatability, quick response time (21 s) and high long-term stability (99%). Therefore, $CoSb_2O_6$ nanospheres can be functionalized as a potential LPG-sensitive material characterized by high sensitivity, reliability and stability at room temperature.

Received 16th July 2020
Accepted 26th August 2020

DOI: 10.1039/d0ra06208a

rsc.li/rsc-advances

Introduction

Liquefied petroleum gas (LPG) is a highly flammable and explosive gas, the use of which as a fuel in various day-to-day applications in homes, hotels, workplaces and industries is increasing worldwide. Therefore, the development of ultra-responsive (fast response time), highly sensitive, robust, long-term stable and trustworthy LPG sensors is necessary for preventing serious accidents.[1–3] These sensors should also be able to operate at room temperature to achieve long-term stability and a simple sensing platform. Therefore, the room temperature sensing of LPG is highly desirable in the sensor research community. In contrast, sensors that operate at high operating temperatures are supported by heaters, which consume significant amount of energy and require a complex sensing platform due to an overall increase in the size and cost of sensors. Additionally, it is obvious that the stability of this type of complex sensing platform is reduced at high operating temperatures, which increases potential issues of reliability and safety of sensors. Besides, sensing at elevated temperatures may lead to changes in the microstructure of the sensing material, which can result in degradation of gas sensing properties with time (*i.e.* long-term stability problem), and due to the explosive nature of LPG, a high operating temperature may also result in an outburst/explosion.[4,5] Therefore, to overcome the above mentioned problems, room temperature LPG sensors are required, which have advantages of low energy consumption, cost effectiveness, device miniaturization (since they are not supported by heaters) and long-term stability. In fact, LPG sensing at room temperature is of major importance from a practical, scientific and technological point of view. Accordingly, the current focus of the sensor community is to develop LPG sensors that exhibit high sensitivity, stability, selectivity and fast response below the lower explosive limit (LEL) of LPG.

There have been significant efforts worldwide to develop LPG sensors having the aforementioned properties.[1–7] Metal oxide nanostructures, such as nanorods, nanocubes, nanowires, nanotetrapods, nanotubes, nanonails, nanobeads, and nanodisks, are the most utilized sensor materials for this purpose.[1–10] However, the major drawbacks of these sensors are their low sensitivity due to low surface adsorption and reactions at room

[a]*Department of Physics, M. P. Government P. G. College, Hardoi-241001, U.P., India. E-mail: satyendra_nano84@rediffmail.com*

[b]*Macromolecular Research Laboratory, Department of Physics, University of Lucknow, Lucknow-226007, U.P., India. E-mail: poonam_tandon@yahoo.co.uk*

[c]*Department of Physics, Government P. G. College, Badaun-243601, U.P., India*

[d]*Department of Applied Physics, Babasaheb Bhimrao Ambedkar University, Lucknow-226025, U.P., India*

temperature. Actually, the sensing properties of sensors are excellent at optimum operating temperatures higher than room temperature.[11–15] Therefore, to increase the surface adsorption (number of oxygen adsorption species) and reactions at room temperature, some researchers have investigated the sensing properties of catalytic materials.[16–20] In this respect, it is known that catalytic materials lead to a significant improvement in sensing properties, and thus can be utilized in gas sensing applications. Catalytic materials are valuable for the fabrication of gas sensors since they increase the number of active sites, and hence, improve the sensing performance and reduce the operating temperature.[16–20] They enhance the number of oxygen active species by adsorbing oxygen molecules on the surface of the sensor, and consequently more oxygen ions are formed on the sensing layers. Therefore, the sensing layers not only facilitate the adsorption of oxygen molecules, but also enhance the formation of oxygen ions by chemical reduction, which then spill on the sensing layers, thus increasing the concentration of O_2^-. Similarly, the test gas can also be directly adsorbed on the surface of catalytic materials to react with pre-adsorbed oxygen ions, as discussed above. These spill-over effects may play a significant role in enhancing the sensing properties of the sensor under investigation. Definitely, the surface interactions are especially vital to the properties of gas sensors, which are translated into electrical signals. Therefore, the role of catalytic materials is very important in the fabrication of gas sensors at room temperature.

Accordingly, nanostructured spinel cobalt oxide (Co_3O_4), a p-type semiconductor material, possesses a narrow optical energy band gap in the range of 1.6–2.2 eV, exists in a mixed valence states of CoO and Co_2O_3, and is well known as good and affordable catalytic material.[21–23] Its potential applications in various fields, *e.g.* catalysis, energy storage, electrochemistry and gas sensors, have been widely reported in the literature.[24–29] Specifically, Co_3O_4 offers many opportunities in the sensing field for the detection of various target gases, such as acetone, toluene, carbon mono-oxide, and ethanol, due to its oxidative catalytic reactivity and noteworthy chemical stability.[21–23,25–29] It has been observed that the most important advantage of Co_3O_4 nanostructures is the variation in their electric properties upon adsorbing on surface species, which may play a key role for enhancing the performance of sensors.[22,23] On the other hand, some investigations also demonstrated the good catalytic properties of antimony oxide (Sb_2O_3) nanostructures.[30,31] Besides, recent results displayed that Sb_2O_3 nanostructures showed reasonable changes in resistance upon exposure to target gases, *i.e.*, the gas and humidity sensing potential of Sb_2O_3 nanostructures has also been presented in the literature.[32,33] Therefore, inspired by the fact that Co_3O_4 and Sb_2O_3 nanostructures have outstanding catalytic properties and high chemical reactivity, we became interested in synthesizing a trirutile-type antimonate material ($CoSb_2O_6$) with excellent potential for gas sensing applications. Actually, based on our recent research, catalytic materials advantageous because they offer the opportunity to be utilized as gas sensors.[34,35] $CoSb_2O_6$ is a p-type semiconducting material having wide band gap of about ~3.7 eV at room temperature, and possesses a trirutile-type crystal structure. This structure is derived from the rutile-type lattice by tripling the *c*-axis. We investigated its LPG sensing properties, which proved that it is an efficient sensing material at room temperature.

As discussed above, nanostructured antimonates are fascinating materials due to their significant photo-catalytic, optical, electrical and sensing properties. Over the last few years, increased attention has been focused on investigating nanostructured antimonates (antimony-based nanostructured oxides having a trirutile-type structure, such as $ZnSb_2O_6$, $CuSb_2O_6$, $MnSb_2O_6$, $NiSb_2O_6$, $MgSb_2O_6$, $CoSb_2O_6$) for gas sensing applications to detect various types of gases.[35–43] In particular, the CO_2 and O_2 gas sensing potential of $CoSb_2O_6$ thick films at 400 °C was investigated by Michel *et al.*[36] Their sensor responded quantitatively to changes in the concentration of CO_2; however, a response towards O_2 was not observed. In another study, Carlos *et al.*[37] reported the CO_2 and CO gas sensing properties of submicron $CoSb_2O_6$ wires operating at 200 °C and 300 °C. Their study revealed that the CO sensor was better than the CO_2 sensor at an operating temperature of 300 °C. The sensitivity of mesoporous $CoSb_2O_6$ nanoparticles to CO and C_3H_8 reported by Bonilla *et al.*[38] was 7.0 and 4.8, respectively, at 350 °C. The dynamic response of $CoSb_2O_6$ trirutile-type oxides in a CO_2 atmosphere was reported by Bonilla *et al.*[39] The sensitivity of their CO_2 sensor at 250 °C was observed to be 3.23 kΩ. In another report[40] by the same group, the sensitivity of a cobalt antimonate pellet was 4.14 at 300 °C for 300 ppm of CO gas. The CO_2 and O_2 sensing properties of $CoSb_2O_6$ microspheres were reported by Michel *et al.*[42] They observed a variation in resistance of 130 Ω and 75 Ω at 400 °C for 400 ppm of CO_2 and O_2, respectively. However, according to the literature, the LPG sensing properties of $CoSb_2O_6$ nanostructures have not been investigated to date. Moreover, the above reported sensing studies were performed at a high operating temperature. Thus, considering these facts, in the present investigation, we report the LPG sensing properties of $CoSb_2O_6$ fabricated from as-grown nanospheres at room temperature for the first time. Room temperature LPG sensing is of significant research interest due to its implication of low energy consumption. Further, the sensing results are discussed in detail, demonstrating the enhanced sensitivity of the $CoSb_2O_6$ thin films at room temperature operation. Long-term stability analyses have also been performed to demonstrate the reproducible nature of the fabricated sensors over time, which show excellent reproducibility. Finally, the obtained results provide an exciting alternative for the highly sensitive, fast responding, stable over a long period and selective detection of LPG, which is an important step in the progress of nanosensor research.

Experimental details

Materials

AR grade cobaltous acetate $(CH_3COO)_2Co\cdot 4H_2O$, antimony trichloride ($SbCl_3$), poly-ethylene glycol (PEG) and ammonium hydroxide (NH_4OH) were purchased from Qualigens, India and

used without further purification. Double distilled water of high quality was used during the synthesis.

Synthesis and growth mechanism of $CoSb_2O_6$

Cobalt antimonate was prepared using cobaltous acetate (0.1 M) and antimony trichloride (0.1 M) in a ratio of 1 : 2, which were dissolved separately in double distilled water under continuous stirring for 6 h at room temperature and then mixed. The pH was adjusted to 9 by adding base (ammonium hydroxide) dropwise. The resultant solution was magnetically stirred at 80 °C for 2 h to obtain a homogeneous solution. Subsequently, 10 mL of poly-ethylene glycol (PEG) was added dropwise, which served as a capping agent. PEG controlled the growth of the particles during the precipitation process. The obtained brown precipitate was dried at 80 °C for 6 h and then ground into a fine powder. Fig. 1(a) illustrates a flow chart of the synthesis of the nanocrystalline cobalt antimonate powder. The as-synthesized powder was annealed at 600 °C for 2 h in an alumina crucible. Further, the prepared crystalline powder was crushed into a fine powder. The resulting powder was pressed uniaxially in a stainless steel die to fabricate $CoSb_2O_6$ pellets (9 mm in diameter and 3 mm in thickness). Thin films of the precursor solution (0.1 M) were fabricated on an alumina substrate (10 × 10 mm^2) using a spin coater (Metrex Scientific Instruments, India) at 2000 rpm for 60 s. The fabricated films were dried at 80 °C for 6 h. This drying process stabilized the films. Further, the films were annealed at 600 °C for 2 h at a heating and cooling rate of 5 °C min^{-1}. This process converted the fabricated films into sensing materials. The thickness of the fabricated films was found to be ~250 nm, which was measured using an Accurion variable angle spectroscopic ellipsometer (Nanofilm EP3 Imaging). Further, the prepared films were investigated upon exposure to different concentrations (in the range of 1000–5000 ppm) of LPG and CO_2 at room temperature.

Fig. 1(b) demonstrates the nucleation and growth mechanism of the cobalt antimonate nanospheres. Initially, in step I, which is considered to be nucleation, the precursor solution, cobaltous acetate and antimony trichloride are self-assembled.[44] In step II, the precursor grows by aggregation involving atom attachment at the growing interfaces[45] to form an intermediate agglomeration-free shape due to the presence of PEG, which functions as a structure-inducing capping agent.[46,47] Further, in the last step (step III), due to the annealing of the material, the intermediate shape is converted into nanospheres, which minimize the overall surface free energy[46] of cobalt antimony oxide.

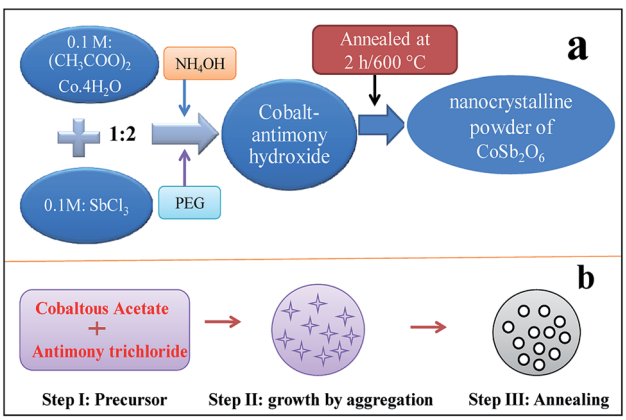

Fig. 1 (a) Flow chart for the synthesis of cobalt antimonate nanospheres and (b) growth mechanism of trirutile $CoSb_2O_6$ nanospheres.

Characterization of $CoSb_2O_6$

The surface morphology of the fabricated thin films annealed at 600 °C was analyzed *via* scanning electron microscopy (SEM, LEO-0430, Cambridge). X-ray powder diffraction (X-Pert PRO PANalytical) was employed for the estimation of the crystallite size and structural analysis of the synthesized material. To identify the chemical bonds in the as-prepared and annealed synthesized materials, FT-IR (Tensor 27) spectra were recorded in the region of 400–4000 cm^{-1}. The optical absorption measurements of the precursor and annealed material were carried out using a UV-visible spectrophotometer (Varian Carry 50 Bio) under ambient conditions.

Gas sensing measurements of $CoSb_2O_6$ thin films

As discussed in the Introduction section, the main aim of this work was to fabricate an efficient LPG sensor that can function at room temperature. Accordingly, a gas sensing chamber was designed, which consisted of an inlet knob for inserting known concentrations of the target gases into the chamber, and an outlet knob for the removal of the stored gas inside the chamber. The gas sensing chamber and measurement process were discussed in detail in our previous publications.[1,48] In brief, the sensors were fabricated in the form of rectangular (12 mm × 18 mm) thin films deposited on alumina substrates *via* the spin-coating process. Silver electrodes were grown on two opposite ends of the films to measure the resistance of the films. Further, the films were inserted into the sensing chamber for the measurements of temporal resistance for different concentrations of the target gas. The concentrations of the target gas were varied in the range of 1000 to 5000 ppm in steps of 1000 ppm, and the corresponding variations in electrical resistance of the sensor were observed for LPG and CO_2 at room temperature (25 °C) and 55% R.H. The sensing properties such as reproducibility and repeated measurements of the same concentrations of the target gases were performed using three different films of $CoSb_2O_6$ fabricated *via* the same procedure. The operating parameters of the fabricated sensors, *e.g.*, sensitivity, selectivity, response and recovery times, reproducibility and long-term stability were evaluated to explain the observed gas sensing performance. The sensitivity of the LPG and CO_2 sensors were defined as follows:[4,47,48]

$$(S)_{LPG} = \frac{R_g}{R_a}; \quad \text{(i)}$$

$$(S)_{CO_2} = \frac{R_g}{R_a} \quad \text{(ii)}$$

where R_a is the stabilized sensor resistance value in air, and R_g is the resistance in the presence of the target gas. The above equations were used to estimate the sensitivity of the fabricated sensors. In addition, the response and recovery times are vital parameters for the rapid detection of dangerous target gases to timely trigger an alarm. The response time is defined as the time taken by the sensor to acquire 90% of its maximum resistance in the presence of the target gas, whereas, the time taken by the sensor to reacquire 10% of the stabilized value of its initial resistance in the absence of the target gas is defined as the recovery time.[4] Besides, the long-term stability of the sensor also plays a key role, which is defined as the repeatability of the sensing measurements at regular intervals for a long run. These parameters were estimated to ensure the potential applicability of the fabricated sensors for the leakage detection of LPG at room temperature.

Results and discussion

Surface morphological and structural analysis

Fig. 2(a) and (b) depict the SEM images of the $CoSb_2O_6$ film at two different scales. Fig. 2(a) and (b) reveal that the nanospheres were uniform in shape. Several nanospheres were highlighted with dotted circles in Fig. 2(a) to calculate their size. The average size of the $CoSb_2O_6$ nanospheres was calculated to be ~45 nm. The observed surface morphology demonstrated numerous active sites, which could facilitate the quick adsorption and reactions of the target gases on their surface, thus enhancing the response of the sensor under investigation. Moreover, the surface morphology was composed of a large numbers of nanospheres, which may play a vital role in enhancing the gas sensing characteristics at room temperature.

Fig. 2(c) presents the X-ray diffraction pattern of the $CoSb_2O_6$ powder annealed at 600 °C. The XRD pattern exhibits strong and sharp peaks, indicating that the synthesized $CoSb_2O_6$ was well crystalline. The (110), (112), (103), (200), (113), (210), (211), (213), (220), (006), (310), (116) and (303) reflection planes observed at 2θ = 27.2°, 31.4°, 34.8°, 36.9°, 38.8°, 40.0°, 44.9°, 53.2°, 56.0°, 59.8°, 63.3°, 66.9° and 67.7°, respectively, correspond to the $CoSb_2O_6$ phase. All the observed planes are in excellent agreement with the standard crystallographic pattern (JCPDS card no. 18-0403) of $CoSb_2O_6$. The crystallite size of $CoSb_2O_6$ was calculated to be 27 nm using the Debye–Scherrer formula, which played a key role in the remarkable and dominant enhancement of LPG sensing.

Michel *et al.*[43] synthesized $CoSb_2O_6$ *via* a solution polymerization method and reported that its thermal decomposition at 700 °C produced $CoSb_2O_6$ with a size of ~50 nm. A two-phase material ($CoSb_2O_6$ together with a minute amount of unreacted Sb_2O_4) was observed by them at 600 °C. In another work by Michel *et al.*,[42] $CoSb_2O_6$ microspheres prepared *via* a colloidal method revealed that calcination at 700 °C produced nearly single-phase $CoSb_2O_6$ (together with some peaks of the secondary phase of $Co_{2.33}Sb_{0.67}O_4$) with a size of ~38 nm. The crystallite size of $CoSb_2O_6$ synthesized *via* the microwave-assisted colloidal method was ~41 nm, as observed by Bonilla *et al.*[39] In another report by Bonilla *et al.*,[38] the crystallite size of $CoSb_2O_6$ synthesized *via* a non-aqueous method was found to be ~41.1 nm. Larcher *et al.*[49] synthesized $CoSb_2O_6$ at a high temperature (800 °C) using a solid-state reaction method. Therefore, according to the comparison of our work with the reported works discussed above, we emphasize here that our adopted method of synthesis produced $CoSb_2O_6$ with a small crystallite size (27 nm). In addition, our results demonstrated that single-phase $CoSb_2O_6$ was obtained at a relatively low temperature (600 °C), which is significantly lower than that reported for $CoSb_2O_6$ using other synthetic methods, as discussed above.[42,43,49] Hence, our observed results in terms of small crystallite size (27 nm), single-phase $CoSb_2O_6$, and formation of trirutile $CoSb_2O_6$ at a relatively low temperature (600 °C) are obviously better than that of previously reported results.[38–40,42,43,49] It is very important to emphasize here that a small crystallite size can play a decisive role in the gas sensing properties of materials.

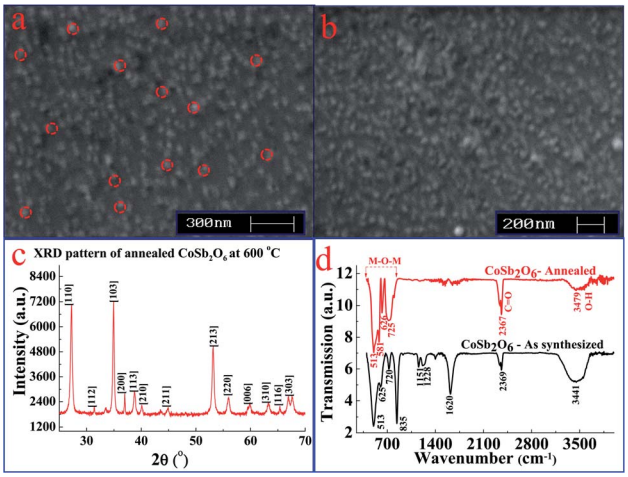

Fig. 2 (a and b) SEM images of annealed $CoSb_2O_6$ film at two different magnifications (dotted circles indicate the nanospheres used for the size calculation), (c) XRD pattern of $CoSb_2O_6$ annealed at 600 °C, and (d) FT-IR spectra of the as-synthesized (pre-annealed) and $CoSb_2O_6$ annealed at 600 °C.

The FT-IR spectra of the pre- and post-annealed cobalt antimonate recorded in the region of 400–4000 cm^{-1} are presented in Fig. 2(d). In the FT-IR spectrum of the annealed $CoSb_2O_6$, the absorption bands (characteristic peak) were observed at 513, 581, 626 and 725 cm^{-1}. These are the characteristic absorption peaks for the M–O–M stretching vibration in $CoSb_2O_6$.[31] The other peaks observed at 2367 and 3479 cm^{-1} are due to the C=O and –OH stretching modes, respectively.[50] The peaks for the as-synthesized (pre-annealed) cobalt antimony oxide were located at 513, 625, 720 and 835 cm^{-1}, which are due to the metal-oxide bonding,[51] and the other peaks observed at 1151, 1228, 1620, 2369 and 3441 cm^{-1} can be assigned to the C–O stretching, N–O stretching, C=O stretching, residual CO_2 and O–H stretching, respectively.[50]

UV-visible absorption analysis

The UV-visible absorption spectra shown in Fig. 3(a) demonstrated the comparative optical absorption of the $CoSb_2O_6$

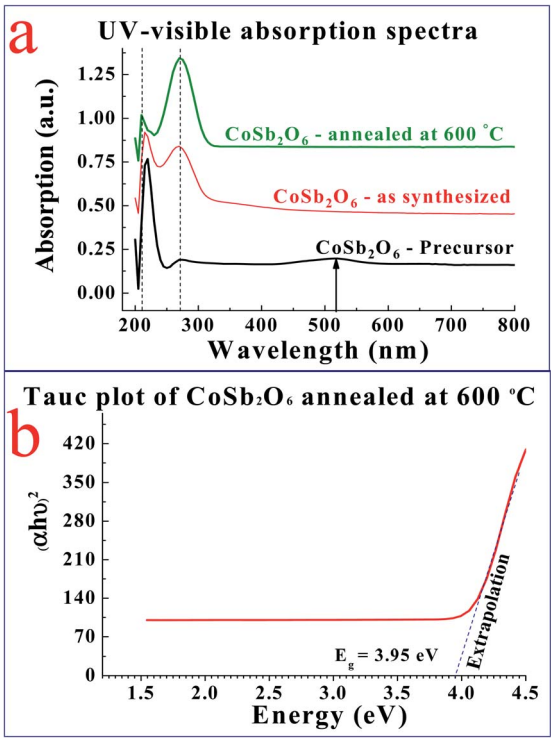

Fig. 3 (a) UV-visible absorption spectra of the precursor, as-synthesized (pre-annealed) and $CoSb_2O_6$ annealed at 600 °C, and (b) Tauc plot for the calculation of the optical band gap of the annealed $CoSb_2O_6$.

precursor, as-synthesized and annealed $CoSb_2O_6$ nanospheres. The absorption spectra revealed slight variations in the absorption peaks of the $CoSb_2O_6$ precursor, as-synthesized and annealed $CoSb_2O_6$ nanospheres. The absorption peak for the annealed $CoSb_2O_6$ was observed at ~270 nm. Furthermore, the spectra did not possess any absorption peaks up to 800 nm, which is consistent with previously reported results.[31] Moreover, the optical absorption peak of $CoSb_2O_6$ reported by Jamal *et al.*[31] was located at ~286 nm, while the absorption peak of Sb_2O_3 observed by Jamal *et al.*[30] was located at 291 nm. However, our results showed an optical absorption peak at slightly lower wavelength (~270 nm), which resulted in the higher optical band gap of the annealed $CoSb_2O_6$.

The optical band gap of the annealed $CoSb_2O_6$ was calculated using the Tauc relation as follows:[17]

$$\alpha h\nu = A(h\nu - E_g)^{1/2} \quad \text{(iii)}$$

where A is a constant, $h\nu$ is the photon energy, E_g is the optical band gap energy and α is the absorption coefficient given by:[17]

$$\alpha = 2.303\left(\frac{A_b}{t}\right) \quad \text{(iv)}$$

In the above equation, A_b is the absorbance and t is the thickness of the cuvette. The plot of $(\alpha h\nu)^2$ *vs.* $h\nu$ is shown by Fig. 3(b). Extrapolation of the linear region of the plot along the x-axis demonstrated the corresponding direct band gap of $CoSb_2O_6$, which was found to be 3.95 eV. Here, it is important to note that the band gap of the synthesized $CoSb_2O_6$ nanospheres was relatively higher compared to that of both the cobalt oxide and antimony oxide.[30,52] This increment in optical band gap may be advantageous considering their sensing applications.

Sensing properties of $CoSb_2O_6$ nanospheres

To investigate the LPG sensing properties of the fabricated $CoSb_2O_6$ films at room temperature, their response upon exposure to different concentrations of LPG in the range of 1000 to 5000 ppm in steps of 1000 ppm was observed, as shown in Fig. 4. The curves observed for different concentrations of LPG illustrated that the resistance increased abruptly initially upon exposure to LPG (response characteristics of the sensor), and remained stable until the opening of the chamber, and finally decreased to a stable value after removing the stored LPG (recovery characteristics of the sensor) in the sensing chamber. Using the definition of sensitivity of the LPG sensor, as

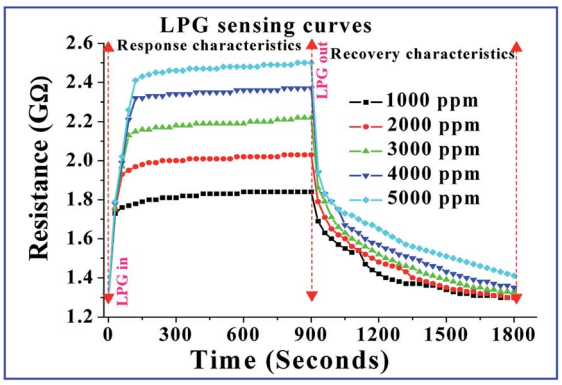

Fig. 4 Variations in the resistance of the cobalt antimonate film with time for different concentrations (1000–5000 ppm) of LPG at room temperature (regions of response and recovery characteristics are shown by dotted lines).

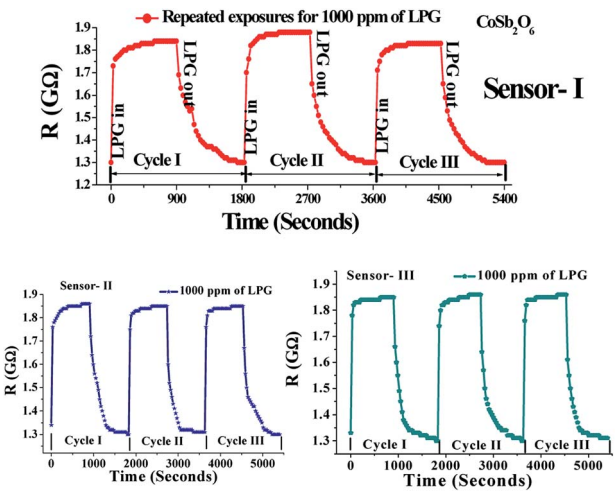

Fig. 5 Repeated measurements (cycles I–III) for three different $CoSb_2O_6$ sensors fabricated using the same procedure for 1000 ppm of LPG.

mentioned in eqn (i), it was also noticeable from the curves that when the LPG was injected into the as-prepared sensor, the sensitivity of the sensor increased sharply, became stable, and then decreased after removing the target gas to attain its original stable value. At lower concentrations of LPG, fewer gaseous molecules were absorbed at the sensing layer, but on increasing the concentration, more oxygen species and LPG molecules were absorbed, resulting in an increase in the sensitivity of the sensor. The maximum sensitivity of the sensor was found to be 1.96 for 5000 ppm of LPG at room temperature. This can be attributed to the fact that the as-prepared cobalt antimonate sensor has numerous active adsorption sites where pre-adsorbed oxygen reacted with LPG, leading to the enhanced sensitivity of the sensor. Besides sensitivity, some aspects such as repeated measurements (multiple cycles) to the same concentrations of LPG, response and recovery times, reproducibility and long-term stability are also important factors for the potential applicability of a sensor. Accordingly, we fabricated three different $CoSb_2O_6$ sensors using the same procedures to measure the above mentioned sensing properties. The multiple resistance switching cycles (repeated exposure for three cycles) for 1000 ppm of LPG are shown in Fig. 5 for three different $CoSb_2O_6$ sensors. All three sensors demonstrated almost the same variations for the repeated measurements, indicating the impressive repeatability.

The reproducibility (2 months after fabrication) was also measured using three different sensors, as discussed above. Their reproducibility curves were plotted by repeating the experiments 2 months after their fabrication for a testing concentration of 5000 ppm of LPG, as shown in Fig. 6. No further variations were found for the reproducibility of the sensing performance, indicating the good reproducibility and stability of the sensors. Besides, the response and recovery times are also very important parameters for a sensor. The response and recovery times of the $CoSb_2O_6$ sensors were found to be ~21 and 234 s, respectively. The response time of the sensor was quite impressive, but its recovery time was long. This long recovery time is attributed to the slow desorption rate of LPG at room temperature. Therefore, the results discussed above (based on the fact that $CoSb_2O_6$ possesses high sensitivity, fast response time, remarkable stability and cost effectiveness) illustrate the good potential of the $CoSb_2O_6$ nanospheres for LPG sensing applications.

We also investigated the $CoSb_2O_6$ films upon exposure to different concentrations of CO_2. The variations in electrical resistance with time for different concentrations of CO_2 (1000–5000 ppm) are shown in Fig. 7(a). All the curves demonstrated that with time, the resistance of the sensing film decreased sharply initially, and afterwards it decreased slowly and finally became saturated. Further, on opening of the outlet of the chamber, the resistance of the film increased sharply and then slowly until it attained a stabilized resistance value in air (R_a) for a further period of time. The response and recovery times of the sensor were found to be ~27 and 26 s, respectively. These values are quite interesting due to the room temperature operation of the sensor. The maximum sensitivity value of the sensor was 1.56, which was obtained for 5000 ppm of CO_2. To examine the stability of the CO_2 sensor, we repeated the sensing experiments for up to 8 weeks.

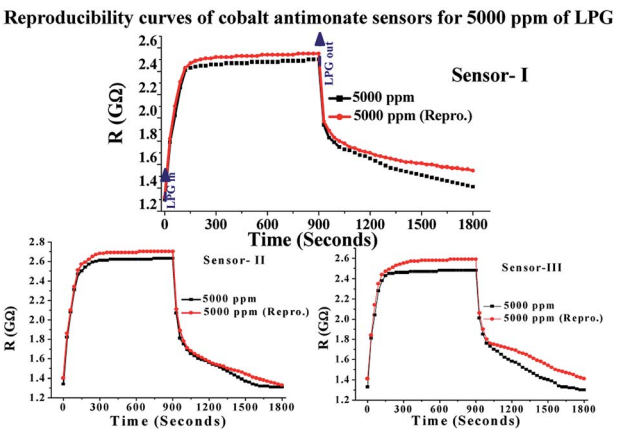

Fig. 6 Reproducibility curves of three different $CoSb_2O_6$ sensors (2 months after fabrication) fabricated using the same procedure for 5000 ppm of LPG at room temperature.

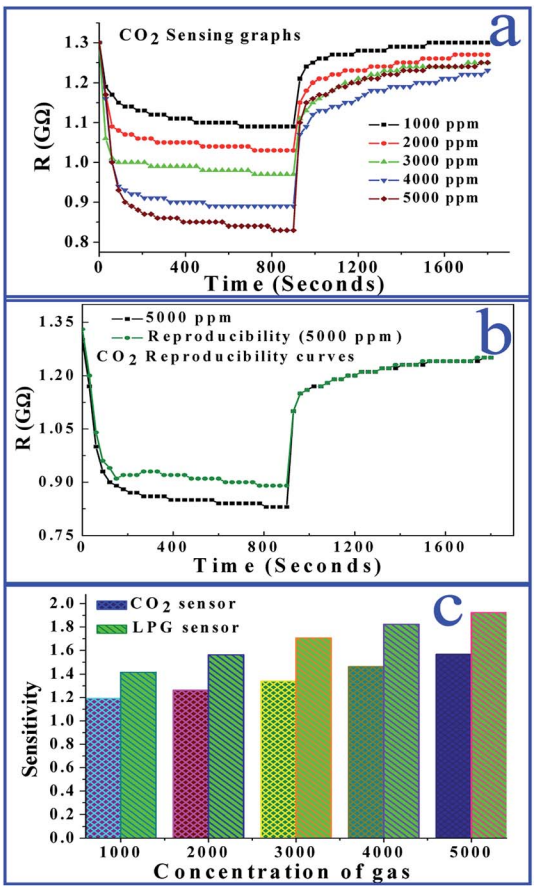

Fig. 7 (a) Dynamic response of $CoSb_2O_6$ film sensor with time for different concentrations (1000–5000 ppm) of CO_2, (b) reproducibility curves of $CoSb_2O_6$ film sensor 2 months after its fabrication for 5000 ppm of CO_2, and (c) comparison of the sensitivity of the sensor for the detection of CO_2 and LPG at room temperature.

The reproducibility curves of the CO_2 sensor shown in Fig. 7(b) demonstrate that the sensing characteristics were reproducible for up to 8 weeks after the fabrication of the sensor. Fig. 7(c) illustrates a comparison of the sensitivity of both sensors. It is obvious that the sensitivity of the LPG sensor is better in comparison to the CO_2 sensor; hence, our film is selective for LPG detection with a fast response time. Therefore, the performance parameters accomplished here by the sensor are appreciable for the leakage detection of the flammable and hazardous LPG. Consequently, our results demonstrate that cobalt antimonate is a promising material for the fabrication of cost-effective and high performance LPG sensors.

For a deeper understanding of the LPG sensing properties, the detailed sensing observations are presented. Additionally, we also examined the LPG sensing capability of Co_3O_4 and Sb_2O_3 nanostructures for the purpose of comparing the observed sensing results. The electrical responses (sensitivity) of the sensors based on $CoSb_2O_6$, Co_3O_4 and Sb_2O_3 films for different concentrations of LPG are compared in Fig. 8(a), among which, the $CoSb_2O_6$ nanospheres display the best electrical response (highest sensitivity) to LPG at room temperature, and thus are very beneficial for the fabrication of sensors. The sensitivity of the sensors fabricated using cobalt oxide, antimony oxide and cobalt antimonate materials was 0.96, 0.46 and 1.96, respectively for 5000 ppm of LPG at room temperature. Thus, the comparative analysis of the sensitivity of the LPG sensors based on $CoSb_2O_6$, Co_3O_4 and Sb_2O_3 demonstrated that $CoSb_2O_6$ showed the highest sensitivity at room temperature. This observed highest sensitivity of $CoSb_2O_6$ at room temperature can be attributed to its catalytic properties and enhanced surface area of its nanosphere structures. Considering the gas sensing application of the sensor, its stability is also a very important parameter, as discussed earlier. The stability of the sensitivity of the sensors to resistance changes is displayed in Fig. 8(b). Three films were prepared and tested to verify the repeatability of the sensing results. Fig. 8(b) demonstrates the long-term stability curves of the fabricated LPG sensors for up to 60 days at a regular interval of 10 days for the cobalt oxide, antimony oxide and cobalt antimonate sensing films when exposed to 1000 ppm of LPG at room temperature. No significant degradation of the sensitivity was observed, and the results clearly indicate that sensor exhibited nearly constant sensitivity for 60 days after its fabrication. In particular, cobalt antimonate enhanced the response of the sensor, while maintaining its stability to resistance changes in the film. Therefore, our present work presents an important improvement with development of a highly sensitive resistive-type LPG sensor. The obtained results demonstrate that the $CoSb_2O_6$ film is a viable LPG-sensitive material at room temperature.

For a better understanding, Fig. 9(a) illustrates a comparison of the sensitivity together with the response time of the sensor materials (cobalt oxide, antimony oxide and cobalt antimonate films) upon exposure to 1000 ppm of LPG. The fastest response

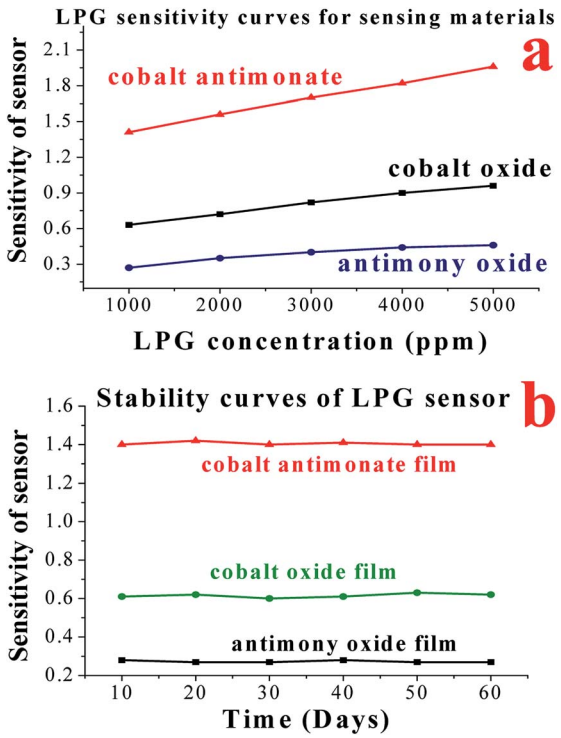

Fig. 8 (a) Comparison of the sensitivity of the fabricated LPG sensor using cobalt oxide, antimony oxide and cobalt antimonate sensing materials, and (b) long-term stability curves of fabricated LPG sensor for up to 60 days at a regular interval of 10 days for cobalt oxide, antimony oxide and cobalt antimonate films when exposed to 1000 ppm of LPG at room temperature.

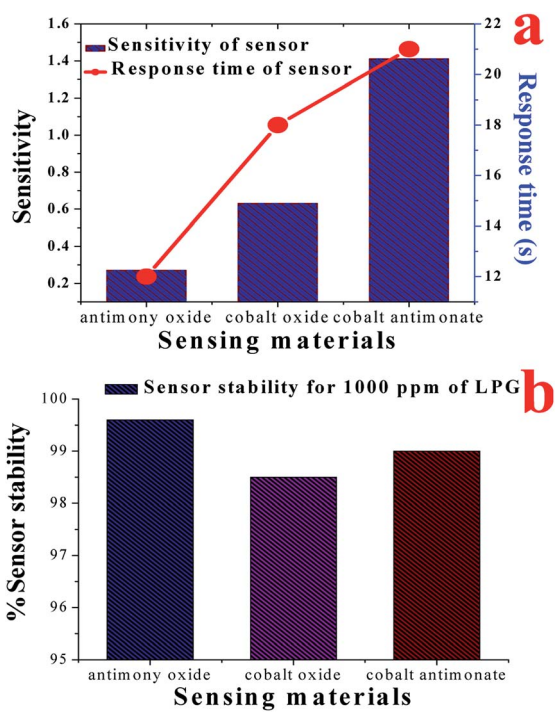

Fig. 9 (a) Comparison of the sensitivity with response time of the sensor materials (cobalt oxide, antimony oxide and cobalt antimonate) upon exposure to 1000 ppm of LPG, and (b) % sensor stability of the fabricated LPG sensor after a long run (60 days) for cobalt oxide, antimony oxide and cobalt antimonate materials at room temperature operation.

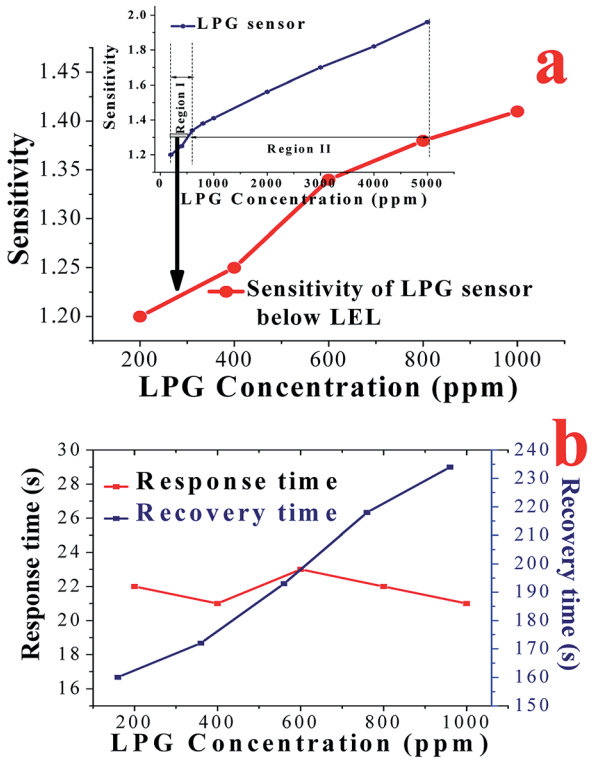

Fig. 10 (a) Sensitivity of cobalt antimonate film sensor as a function of different concentrations (200–1000 ppm) of LPG (sensitivity in the whole concentration range of LPG, *i.e.*, 200–5000 ppm displayed in the inset), and (b) response and recovery times of the sensor upon exposure of different concentrations (200–1000 ppm) of LPG below its lower explosive limit.

time (12 s) was observed for the Sb_2O_3 film, but its sensitivity (0.46) was also the lowest. The response time and sensitivity of Co_3O_4 film were 18 s and 0.96, respectively. However, in the case of $CoSb_2O_6$ these values were 21 s and 1.96, respectively. Indeed, it was very difficult to select the most suitable material among the investigated films as an LPG sensor since we could choose either a faster response or higher sensitivity, which were not achieved simultaneously for any of the films. A short response time and high sensitivity indeed play a very important role in gas sensing applications. However, although Sb_2O_3 demonstrated the fastest response time (12 s), it also had the lowest LPG response among the materials. Therefore, $CoSb_2O_6$ demonstrated the best potential for LPG detection since it exhibited the highest sensitivity (1.96) among them, together with a significantly short response time (21 s). Additionally, we cannot ignore that the sensitivity of the $CoSb_2O_6$-based LPG sensor is the highest together with the fastest response time among the LPG sensors reported to date, which is the highest sensitivity value at room temperature operation for a sensor. The long-term stability of the sensors was examined for 60 days, and tested at an interval of 10 days. These results are presented in Fig. 9(b) for the cobalt oxide, antimony oxide and cobalt antimonate sensing materials at room temperature. The fabricated Co_3O_4, Sb_2O_3 and $CoSb_2O_6$ sensors exhibited 98.5%, 99.6% and 99% stability for up to 60 days, respectively. These results demonstrate that $CoSb_2O_6$ was highly stable over a measurement period of 60 days, with a loss in sensitivity of ~1%. Thus, the obtained results prove that $CoSb_2O_6$ presents a promising platform as an LPG sensor at room temperature, especially due to its low cost and highly stable response. Hence, it can be argued that the cobalt antimonate sensor provides promising insight into the design and fabrication of room temperature LPG sensors.

As discussed above, the $CoSb_2O_6$ nanospheres show very promising potential for the detection of LPG leakage in the concentration range of 1000–5000 ppm. Thus, to examine the behaviour of the sensor below the lower explosive limit (LEL) of LPG, its sensing characteristics were also investigated below the LEL (1000 ppm). Fig. 10(a) demonstrates the sensitivity of the cobalt antimonate film sensor as a function of different concentrations (200–1000 ppm at an interval of 200 ppm) of LPG below its LEL. The variation in the sensitivity of the sensor in the whole LPG concentration range, *i.e.*, 200–5000 ppm is displayed in the inset of Fig. 10(a). The inset has two regions of different slopes, where region I from 200–600 ppm is steeper (highly sloped) than region II (800–5000 ppm). Therefore, it is obvious that the sensitivity of the sensor increased rapidly and linearly up to 600 ppm with a high slope and then increased slowly with a different slope up to 5000 ppm of LPG. The

Table 1 Overview of the sensing properties of previously reported antimonate-based gas sensors

S. no.	Sensing material	Synthesis method	Size of material	Target gas	Conc. of gas	Operating temperature	Sensitivity	Ref.
1	$CoSb_2O_6$	Non-aqueous	41 nm	C_3H_8	300 ppm	350 °C	4.80	38
2	$CoSb_2O_6$	Colloidal	41 nm	CO_2	0.100 sccm	300 °C	1.29 kΩ	39
3	$CoSb_2O_6$	Colloidal	18 nm	CO	300 ppm	300 °C	4.14	40
4	$CoSb_2O_6$	Microwave radiation	38 nm	CO_2	400 ppm	400 °C	130 Ω	42
5	$NiSb_2O_6$	Colloidal	31.2 nm	C_3H_8	500 ppm	300 °C	1.10	53
6	$NiSb_2O_6$	Wet chemical	40 nm	C_3H_8	500 ppm	23 °C	1.3	54
7	$NiSb_2O_6$	Wet-chemistry	46 nm	CO	300 ppm	300 °C	0.35	55
8	$MgSb_2O_6$	Colloidal	20 nm	C_3H_8	300 ppm	250 °C	52.20	56
9	$MnSb_2O_6$	Colloidal	29.5 nm	C_3H_8	500 ppm	300 °C	0.44	57
10	$ZnSb_2O_6$	Solution	50–250 nm	C_3H_8	300 ppm	250 °C	1.26	58
11	**$CoSb_2O_6$**	**Sol–gel**	**27 nm**	**LPG**	**5000 ppm**	**25 °C**	**1.96**	**Present work**

Table 2 Comparison of response time of antimonate-based room temperature LPG sensors

S. no.	Antimonate material	LPG concentration	Response time	Ref.
1	$NiSb_2O_6$ nanospheres	1000 ppm	100 s	59
2	$ZnSb_2O_6$ nano-cubes/ cuboids	1000 ppm	41 s	34
3	$CuSb_2O_6$ nanopolygons	1000 ppm	25 s	35
4	$CoSb_2O_6$ nanospheres	1000 ppm	21 s	Current work

response and recovery times of the sensor upon exposure to different concentrations (200–1000 ppm) of LPG are shown in Fig. 10(b). The lowest values were 22 and 160 s, respectively, observed for 200 ppm of LPG. Thus, according to the experimental data presented in Fig. 10(a) and (b), it is obvious that the sensor responded to a much lower concentration than the LEL of LPG with a fast response time (22 s), indicating that the synthesized $CoSb_2O_6$ nanospheres are extraordinary for the construction of LPG sensors. Interestingly, this type of sensor will be very helpful for tracing the leakage of low concentrations of LPG below its LEL. In addition to their LPG sensing properties, other interesting applications, such as humidity and optoelectronic humidity sensing properties, were worth investigating for the $CoSb_2O_6$ nanospheres.

Many earlier studies demonstrated that antimonates were applied as sensors, as discussed in the Introduction. Thus, it was also of interest to compare and discuss our results with that obtained previously for antimonate materials. Table 1 presents a brief overview of nanostructured antimonates for the sensing of various gases.[38–40,42,53–58] According to the summarized data presented in Table 1, we observed that the antimonate sensors reported in the literature have an optimum operating temperature of about 200 °C. However, in our case, the operating temperature was room temperature (25 °C), and consequently, the dynamic response of the sensor was quite stable for over 2 months. Thus, for the first time, we reported the high sensitivity (1.96) of $CoSb_2O_6$ at room temperature towards the detection of LPG in comparison with the data available in the literature. We also emphasized the operating temperature (25 °C) at which the sensing characteristics were examined in our study. Further, the sensor community has focused their attention on the development of LPG sensors, but the room temperature operation of LPG sensors is still a challenge due to the large response and recovery time values. Accordingly, to improve the response and recovery times, catalytic materials are very beneficial. They play a very prominent role in improving the response time of sensors. Table 2 compares the response time of the $CoSb_2O_6$ sensor developed in the current work with recently reported antimonate-based LPG sensors.[34,35,59] It can be concluded from the table that $CoSb_2O_6$ responds the fastest to LPG among the reported sensors based on catalytic materials. Thus, it is necessary to emphasize here that the lowest response time value at room temperature is an important feature of the present sensor. Besides, the high stability and repeatability indicate the efficiency of the p-type $CoSb_2O_6$ sensor for the leakage detection of LPG. Therefore, we consider that the presented results will be of great interest for the development of highly sensitive p-type $CoSb_2O_6$ sensors even below the LEL of LPG.

To date, many efforts have been devoted to the fabrication of LPG sensors that operate at room temperature. Here, only the recently reported most relevant LPG-sensitive materials for detection at room temperature are summarized for a comparison with our observed sensing results, as presented in Table 3. This table can offer motivation to general readers. In brief, Pasha *et al.*[60] reported a highly sensitive ethylene glycol-doped PEDOT-PSS (poly 3,4-ethylenedioxythiophene:polystyrene sulfonate) organic thin film sensor for the detection of LPG at room temperature. They demonstrated that 20 wt% ethylene glycol-doped PEDOT-PSS exhibited the highest sensitivity of 0.91 with a response time of 8.45 min and recovery time of 12.75 min at a concentration of 20 000 ppm of LPG. Goutham *et al.*[61] demonstrated an LPG sensor at room temperature (27 °C) based on a CdO/graphene nanocomposite with a maximum response of 0.77 upon exposure to 600 ppm of LPG. Reddy *et al.*[62] investigated an MgO–CeO_2 nanocomposite for the leakage detection of LPG at room temperature. The sensor

Table 3 Comparison of the performance of the $CoSb_2O_6$ sensor with other room temperature LPG sensors recently reported in the literature

S. no.	Sensing material	Conc. of LPG (ppm)	Sensitivity	Response time	Recovery time	Year of publication	Ref.
1	Ethylene glycol-doped PEDOT-PSS	20 000	0.91	8.45 min	12.75 min	2018	60
2	CdO/graphene	600	0.77	—	—	2019	61
3	MgO–CeO_2	900	0.32	—	—	2019	62
4	ZnO/poly-pyrrole/PbS QDs	1000	0.45	—	—	2019	63
5	CdS : SiO_2	1000	0.71	91 s	140 s	2019	2
6	$ZnSb_2O_6$	1000	1.36	41 s	95 s	2020	34
7	$CuSb_2O_6$	1000	1.49	25 s	180 s	2020	35
8	**$CoSb_2O_6$**	**200**	**1.20**	**22 s**	**160 s**	**Current work**	**Current work**

demonstrated good selectivity towards LPG with a sensitivity of 0.32 at 900 ppm. The Zhang *et al.*[63] fabricated a room temperature LPG sensor based on zinc oxide/poly-pyrrole/lead sulfide quantum dots having a maximum sensitivity 0.45 at 1000 ppm of LPG. Innovatively, Saxena *et al.*[2] prepared CdS nanodroplets over silica microballs for the development of a room temperature LPG sensor. Their highest sensitivity value was 0.71 for 1000 ppm of LPG at room temperature with the response and recovery times of 91 and 140 s, respectively. Our group[34,35] recently investigated the LPG response of $ZnSb_2O_6$ nano-cubes/cuboids and $CuSb_2O_6$ nanopolygons. Their sensitivities were 1.36 and 1.49, respectively for 1000 ppm of LPG. However, in the present work, the sensitivity of the $CoSb_2O_6$ sensor was 1.20 having a response time 22 s at a considerably lower concentration of LPG (200 ppm). A careful inspection of Table 3 indicates that our sensor even at low concentrations of LPG possesses a relatively enhanced LPG sensing performance in comparison with all the previously reported sensors. Therefore, our sensor is superior among the other room temperature sensors in terms of its highest sensitivity value, fast response time and highly reproducible and stable behaviour. The potential sensing of LPG below its LEL suggests that $CoSb_2O_6$ has further scope toward industrial applications, and hence a progressive step towards the development of LPG sensors.

Sensors based on catalytic nanostructured materials not only exhibit enhanced sensitivity, but also significantly improved (decreased) response time and optimum operating temperature.[16–20] At the sensing layers, the chemical reaction of the target gas molecules occurs during gas adsorption with pre-adsorbed oxygen species.[16–20] The sensor based on Sb_2O_3 facilitated a quick adsorption and reaction, and hence showed the fastest response time among the investigated sensors. These features demonstrated the quick adsorption of gas at the surface. Surface interactions such as gas adsorption and reactions are based on catalytic reactions. The adsorption/desorption of the target gas molecules on the sensing layers developed the reaction process and could exchange the electrons from the surface adsorbed oxygen species O_2^-. These electrons are responsible for the variations in the electrical resistance of the sensing layer, thereby, enhancing and promoting the changes in the depletion layer. These variations in resistance are a crucial parameter for the determination of the gas sensing properties.

The operation of the antimonate-based resistive nanosensor is based on the modulation in the electrical resistance of its sensing layer due to its interaction (adsorption and reactions) with the target gas molecules. The sensing layer usually determines the gas sensing properties, *i.e.*, the sensing materials and the structures of the sensing layers play a crucial role in the sensing performance. To measure the gas sensing properties, initially the sensing film was stabilized in air for ~10 min. During this process, it adsorbed oxygen from the air on the surface of the sensor. These absorbed oxygen molecules captured electrons from the conduction band of the antimonate surface, resulting in the formation of negatively charged chemisorbed oxygen ions, O_2^-, at room temperature operation. Consequently, the density of hole carriers increased and an accumulated hole layer was formed on the sensing surface, due to which a potential barrier was generated. Therefore, the resistance of the sensing film decreased, and after some time (~10 min), it became saturated. The reaction kinematics during the stabilization process can be explained by the following chemical reactions:[4,13]

$$O_2(gas) \leftrightarrow O_2(ads) \quad (v)$$

$$O_2(ads) + e^- \rightarrow O_2^- \quad (vi)$$

After attaining a stabilized value of resistance in air (R_a), the sensor was exposed to different concentrations of LPG in a controlled manner. In this process, the alkanes diffused through the sensing film and reacted with the pre-adsorbed ionic oxygen species on the antimonate surface. Upon chemical reaction with the pre-adsorbed ionic oxygen species, the alkanes eventually break down into CO_2 and H_2O.[4] Once LPG was in the on state, the electrons trapped by the oxygen species would be released since the chemical reaction releases electrons, which finally neutralized the conduction carriers (holes) of the p-type $CoSb_2O_6$ very quickly. Consequently, the hole accumulating layer was reduced, causing a drastic increase in the resistance of the film under investigation. Consequently, a potential barrier to charge transport developed, and further the resistance became constant, as can be seen in Fig. 4. A schematic of the above LPG sensing mechanism is displayed in Fig. 11. In step I, atmospheric oxygen was adsorbed on the surface of the sensing film. In step II, the adsorbed O_2 reacted with the oxygen of $CoSb_2O_6$ and extracted electrons from its conduction band, thereby forming O_2^-. This step produced a stabilized electrical resistance for the film in air (R_a). In step III, when LPG was exposed to the sensing layer, alkanes (C_nH_{2n+2}) reacted with O_2^-, and finally in step IV, a number of electrons were ejected due to the chemical interactions, which

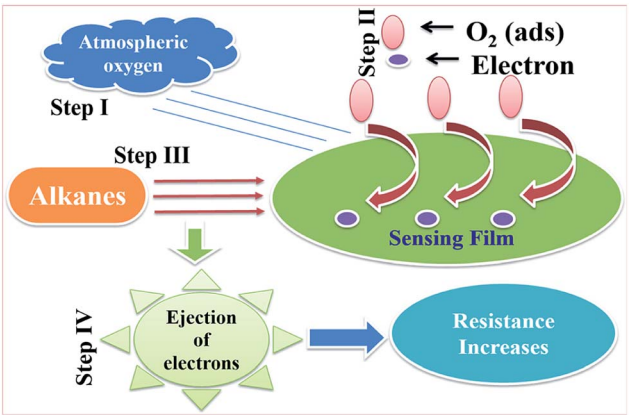

Fig. 11 Schematic of LPG sensing mechanism (step I: adsorption of atmospheric oxygen on the surface of the sensing film; step II: adsorbed oxygen species react with the sensing material, resulting in the stable electrical resistance of the film; step III: LPG is exposed to the sensing layers and interactions between the alkanes and adsorbed species occur; and finally, step IV: ejection of charge carriers due to the chemical interactions, which are responsible for the modulation of resistance of the film under investigation).

were responsible for the modulation of the electrical resistance of the film. Oxygen (O_2^-) could be created more efficiently on the surface of $CoSb_2O_6$, resulting in an enhancement in the response of the sensor and decrease in its response time. The enhancement in sensitivity was mainly due to the increase in the width of the conduction channel (reduced barrier height), as discussed above.

In summary, trirutile $CoSb_2O_6$ demonstrated superior LPG sensing properties at room temperature considering its high sensitivity, fast response time and interesting long-term stability properties, thus providing potential for the development of LPG sensors. Another important finding was that the LPG response of the $CoSb_2O_6$ film at room temperature was enhanced compared to that in previously reported work, which is the progress achieved by our group. The fabricated $CoSb_2O_6$ presents an alternative material with highly sensitive and stable sensing properties, which can be beneficial in the area of public security and industrial applications. Thus, these findings open up new perspectives for antimonates in the design and fabrication of room temperature gas sensing materials, which can be efficiently utilized in the detection of LPG.

Conclusions

An efficient sensor fabricated using $CoSb_2O_6$ thin films for the detection of LPG at room temperature was reported for the first time. $CoSb_2O_6$ nanospheres were successfully synthesized *via* a sol–gel spin-coating method and characterized for their structural and morphological features. The process used herein was convenient, environmentally friendly, inexpensive and efficient for the preparation of the sensor. The response of the fabricated sensors was studied upon exposure to LPG and CO_2 gas at room temperature, which displayed proficient sensing behaviour to LPG. The stability study indicated that the sensor retained its initial response over a period of 60 days, where its sensing response was highly stable (deterioration of ~1% in 60 days). Besides the above mentioned relevant results, the outstanding feature of the sensor is that it operated at room temperature (25 °C). Therefore, the developed sensor in the current work is highly promising due to its high sensitivity (1.96), low detection limit (200 ppm), short response time (21 s), impressive reproducibility and stability (99%), and simple fabrication, especially towards the detection of LPG at room temperature. Therefore, we strongly believe that the demonstrated $CoSb_2O_6$ is a good candidate as an LPG sensor. Furthermore, the fabricated sensor is unique since it detected the leakage of LPG below its LEL (200 ppm) with a significantly fast response, and hence offers industrial applications.

Conflicts of interest

There are no conflicts to declare.

Acknowledgements

This research did not receive any specific grant from funding agencies in the public, commercial, or not-for-profit sectors.

References

1 A. K. Jaiswal, S. Singh, A. Singh, R. R. Yadav, P. Tandon and B. C. Yadav, *Mater. Chem. Phys.*, 2015, **154**, 16–21.
2 N. Saxena, P. Kumar and V. Gupta, *Nanoscale Adv.*, 2019, **1**, 2382–2391.
3 R. K. Mishra, S. B. Upadhyay, A. Kushwaha, T. H. Kim, G. Murali, R. Verma, M. Srivastava, J. Singh, P. P. Sahay and S. H. Lee, *Nanoscale*, 2015, **7**, 11971–11979.
4 Z. Li, H. Li, Z. Wu, M. Wang, J. Luo, H. Torun, *et al.*, *Mater. Horiz.*, 2019, **6**, 470–506.
5 A. Singh, A. Singh, S. Singh, B. C. Yadav and P. Tandon, *J. Alloys Compd.*, 2015, **618**, 475–483.
6 S. S. Nkosi, I. Kortidis, D. E. Motaung, R. E. Kroon, N. Leshabane, J. Tshilongo and O. M. Ndwandwe, *Mater. Chem. Phys.*, 2020, **242**, 12242.
7 K. K. Dey, D. Bhatnagar, A. K. Srivastava, M. Wan, S. Singh, R. R. Yadav, B. C. Yadav and M. Deepa, VO_2 nanorods for efficient performance in thermal fluids and sensors, *Nanoscale*, 2015, **7**, 6159–6172.
8 D. Gedamu, I. Paulowicz, S. Kaps, O. Lupan, S. Wille, G. Haidarschin, Y. K. Mishra and R. Adelung, *Adv. Mater.*, 2014, **26**, 1541–1550.
9 S. Saritas, M. Kundakci, O. Coban, S. Tuzemen and M. Yildirim, *Phys. B*, 2018, **541**, 14–18.
10 O. Lupan, V. Postica, J. Gröttrup, A. K. Mishra, N. H. De Leeuw, J. F. C. Carreira, J. Rodrigues, N. Ben Sedrine, M. R. Correia, T. Monteiro, V. Cretu, I. Tiginyanu, D. Smazna, Y. K. Mishra and R. Adelung, *ACS Appl. Mater. Interfaces*, 2017, **9**, 4084–4099.
11 Z. Dai, T. Liang and J. H. Lee, *Nanoscale Adv.*, 2019, **1**, 1626–1639.
12 R. Malik, V. K. Tomer, Y. K. Mishra and L. Lin, *Appl. Phys. Rev.*, 2020, **7**, 021301–021399.
13 L. Ge, X. Mu, G. Tian, Q. Huang, J. Ahmed and Z. Hu, *Front. Chem.*, 2019, **7**, 839.
14 V. Cretu, V. Postica, A. K. Mishra, M. Hoppe, I. Tiginyanu, Y. K. Mishra, L. Chow, N. H. de Leeuw, R. Adelung and O. Lupan, *J. Mater. Chem. A*, 2016, **4**, 6527–6539.
15 H. Ji, W. Zeng and Y. Li, *Nanoscale*, 2019, **11**, 22664–22684.
16 B. Zhang, M. Cheng, G. Liu, Y. Gao, L. Zhao, S. Li, Y. Wang, F. Liu, X. Liang, T. Zhang and G. Lu, *Sens. Actuators, B*, 2018, **263**, 387–399.
17 S. Singh, A. Singh, B. C. Yadav and P. K. Dwivedi, *Sens. Actuators, B*, 2013, **177**, 730–739.
18 T. Zhang, X. Tang, J. Zhang, T. Zhou, H. Wang, C. Wu, X. Xia, C. Xie and D. Zeng, *Langmuir*, 2018, **34**, 14577.
19 A. Singh, S. Singh, B. D. Joshi, A. Shukla, B. C. Yadav and P. Tandon, *Mater. Sci. Semicond. Process.*, 2014, **27**, 934–950.
20 Z. Zhang, Z. Wen, Z. Ye and L. Zhu, *RSC Adv.*, 2015, **5**, 59976–59982.
21 Q. Zhou and W. Zeng, *Phys. E*, 2018, **95**, 121–124.
22 X. Wang, W. Tian, T. Zhai, C. Zhi, Y. Bando and D. Golberg, *J. Mater. Chem.*, 2012, **22**, 23310–23326.
23 S. Wicker, K. Grosmann, N. Barsan and U. Weimar, *Sens. Actuators, B*, 2013, **185**, 644–650.

24 S. Sun, X. Zhao, M. Yang, L. Wu, Z. Wen and X. Shen, *Sci. Rep.*, 2016, **6**, 19564–19573.
25 P. Kannan, T. Maiyalagan, E. Marsili, S. Ghosh, L. Guo, Y. Huang, J. A. Rather, D. Thiruppathi, J. N. Jönsson and M. J. Niedziolka, *Analyst*, 2017, **142**, 4299–4307.
26 Q. Ren, S. Mo, R. Peng, Z. Feng, M. Zhang, L. Chen, M. Fu, J. Wu and D. Ye, *J. Mater. Chem. A*, 2018, **6**, 498–509.
27 J. Deng, L. Wang, Z. Lou and T. Zhang, *RSC Adv.*, 2014, **4**, 21115–21120.
28 T. Liu, J. Liu, Q. Liu, Y. Sun, X. Jing, H. Zhang and J. Wang, *CrystEngComm*, 2016, **18**, 5728–5735.
29 J. Cao, S. Wang, J. Li, Y. Xing, X. Zhao and D. Li, *Sens. Actuators, B*, 2020, **315**, 128120.
30 A. Jamal, M. M. Rahman, M. Faisal and S. B. Khan, *Mater. Sci. Appl.*, 2011, **2**, 676–683.
31 A. Jamal, M. M. Rahman, S. B. Khan, M. Faisal, K. Akhtar, M. A. Ru, A. M. Asiri and A. O. Al-Youbi, *Appl. Surf. Sci.*, 2012, **261**, 52–58.
32 K. Suematsu, M. Sasaki, N. Ma, M. Yuasa and K. Shimanoe, *ACS Sens.*, 2016, **1**, 913–920.
33 C. Schoendorfer, M. Hetzel, P. Pongratz, A. Lugstein and E. Bertagnolli, *Nanotech*, 2012, **23**, 435502–435508.
34 S. Singh, A. Singh, A. Singh and P. Tandon, *RSC Adv.*, 2020, **10**, 20349–20357.
35 S. Singh, A. Singh, A. Singh and P. Tandon, *New J. Chem.*, 2020, **44**, 11949–11958.
36 C. R. Michel, A. H. Martínez and J. P. Morán, *Sens. Actuators, B*, 2009, **140**, 149–154.
37 M. Carlos, A. H. M. Preciado and N. L. L. Contreras, *Sens. Lett.*, 2012, **10**, 8–13.
38 H. G. Bonilla, L. G. Ortiz, M. O. Amador, J. S. Salazar, V. M. R. Betancourtt, A. G. Bonilla and J. R. Gomez, *J. Nanomater.*, 2015, **2015**, 308465.
39 A. G. Bonilla, V. M. R. Betancourtt, M. F. Martínez, O. B. Alonso, J. R. Gómez, L. G. Ortiz and H. G. Bonilla, *Sensors*, 2014, **14**, 15802–15814.
40 A. G. Bonilla, O. B. Alonso, J. T. G. Bonilla, M. L. O. Amador, V. M. R. Betancourtt, A. S. Martínez, J. P. M. Lázaro, M. M. García and H. G. Bonilla, *J. Mater. Sci.: Mater. Electron.*, 2018, **29**, 15632–15642.
41 A. G. Bonilla, V. M. R. Betancourtt, H. G. Bonilla, L. G. Ortiz, O. B. Alonso, N. E. F. Rodríguez, J. R. Gómez, A. C. Zamora and J. T. G. Bonilla, *J. Mater. Sci.: Mater. Electron.*, 2018, **29**, DOI: 10.1007/s10854-018-9228-4.
42 C. R. Michel, H. G. Bonilla, A. H. M. Preciado and J. P. M. Lázaro, *Sens. Actuators, B*, 2009, **143**, 278–285.
43 C. R. Michel, A. H. Martínez and S. Jiménez, *Sens. Actuators, B*, 2008, **132**, 45–51.
44 N. T. K. Thanh, N. Maclean and S. Mahiddine, *Chem. Rev.*, 2014, **114**, 7610–7630.
45 F. Wang, V. N. Richards, S. P. Shields and W. E. Buhro, *Chem. Mater.*, 2014, **26**, 5–21.
46 B. Viswanath, P. Kundu, A. Halder and N. Ravishankar, *J. Phys. Chem. C*, 2009, **113**, 16866–16883.
47 S. Singh, A. Singh, R. R. Yadav and P. Tandon, *Mater. Lett.*, 2014, **131**, 31–34.
48 D. A. Pomogailo, S. Singh, M. Singh, B. C. Yadav, P. Tandon, S. I. Pomogailo, G. I. Dzhardimalieva and K. A. Kydralieva, *Inorg. Mater.*, 2014, **50**, 296–305.
49 D. Larcher, A. S. Prakash, L. Laffont, M. Womes, J. C. Jumas, J. O. Fourcade, M. S. Hedge and J. M. Tarascon, *J. Electrochem. Soc.*, 2006, **153**, A1778–A1787.
50 D. L. Pavia, G. M. Lampman and G. S. Kriz, Infrared and Raman Spectrometries: vibrational Spectrometries, 1987, ch. 10, p. 468.
51 F. A. Miller and C. H. Wilkins, *Anal. Chem.*, 1952, **24**, 1253–1294.
52 B. C. Yadav, R. C. Yadav, S. Singh, P. K. Dwivedi, H. Ryu and S. Kang, *Opt. Laser Technol.*, 2013, **49**, 68–74.
53 V. M. R. Betancourtt, H. G. Bonilla, M. F. Martínez, A. G. Bonilla, J. P. M. Lazaro, J. T. G. Bonilla, M. A. Gonzalez and M. L. O. Amador, *J. Nanomater.*, 2017, **2017**, 1–9.
54 H. G. Bonilla, M. L. O. Amador, Y. L. C. Moreno, J. T. G. Bonilla, A. G. Bonilla, L. G. Ortiz, J. P. M. Lazaro, J. S. Salazar and V. M. R. Betancourtt, *J. Mater. Sci.: Mater. Electron.*, 2019, **30**, 6166–6177.
55 J. T. G. Bonilla, H. G. Bonilla, V. M. R. Betancourtt, A. C. Zamora, J. A. R. Ortega, L. G. Ortiz, M. E. S. Morales, O. B. Alonso and A. G. Bonilla, *Appl. Sci.*, 2019, **9**, 3799–3815.
56 H. G. Bonilla, M. F. Martinez, V. M. R. Betancourtt, A. G. Bonilla, J. R. Gomez, L. G. Ortiz, M. L. O. Amador and J. S. Salazar, *Sensors*, 2016, **16**, 177.
57 H. G. Bonilla, V. M. R. Betancourtt, J. T. G. Bonilla, L. G. Ortiz, A. G. Bonilla, Y. L. C. Moreno, O. B. Alonso and J. R. Gomez, *Sensors*, 2018, **18**, 2299–2315.
58 H. G. Bonilla, V. M. R. Betancourtt, J. T. G. Bonilla, J. R. Gómez, L. G. Ortiz, M. F. Martínez, M. L. O. Amador and J. S. Salazar, *J. Nanomater.*, 2015, **2015**, 979543, DOI: 10.1155/2015/979543.
59 A. Singh, A. Singh, S. Singh and P. Tandon, *Chem. Phys. Lett.*, 2016, **646**, 41–46.
60 A. Pasha, S. Khasim, O. A. Al-Hartomy, M. Lakshmi and K. G. Manjunatha, *RSC Adv.*, 2018, **8**, 18074–18083.
61 S. Goutham, N. Jayarambabu, C. Sandeep, K. K. Sadasivuni, D. S. Kumar and K. V. Rao, *Microchim. Acta*, 2019, **6**, 861–869.
62 M. S. B. Reddy, S. Kailasa, B. G. Rani, N. Jayarambabu, K. Bikshalu, P. Munindra and K. V. Rao, *J. Mater. Sci.: Mater. Electron.*, 2019, **30**, 17295–17302.
63 D. Zhang, G. Dong, Z. Wu, W. Pan and X. Fan, *IEEE Sens. J.*, 2019, **19**, 2855–2862.